Biointerface Research in Applied Chemistry
Open-Access Journal (ISSN: 2069-5837)

Article
Volume 16, Issue 1, 2026, 16
https://doi.org/10.33263/BRIAC161.016

Targeting Breast Cancer with Schiff Base Metal Complexes: Synthesis, Structural Characterization, and In-Vitro/In-Silico Validation

Chethana Mysore Harishwara [1], Priyadarshini A N [2,3], Ningaraju Gejjiganahalli Ningappa [1], Sudhanva Muddenahalli Srinivasa [2,3], Shobith Rangappa [2,3], Mallu Puttaswamappa [1,*]

[1] Department of Chemistry, SJCE, JSS Science and Technology University, Mysuru-570 006, Karnataka, India
[2] Adichunchanagiri Institute for Molecular Medicine, Adichunchanagiri Institute of Medical Sciences, Adichunchanagiri University, BG Nagara-571448 Karnataka, India
[3] School of Natural Sciences, Adichunchanagiri University, BG Nagara-571448 Karnataka, India
* Correspondence: pmallu@jssstuniv.in;

Received: 28.08.2025; Accepted: 18.11.2025; Published: 15.02.2026

Abstract: A novel bidentate Schiff base ligand (HL), derived from dopamine and 1,4-benzodioxane-6-carboxaldehyde, was employed for the microwave-assisted synthesis of a new series of transition metal complexes: $Cu(HL)_2$, $Co(HL)_2$, $Ni(HL)_2$, and $Zn(HL)_2$. The rapid, solvent-efficient synthesis yielded high-purity products, which were comprehensively characterized by spectroscopic, diffraction, and thermal analyses. Spectroscopic data confirmed the bidentate coordination of HL via the phenolic oxygen atoms. Among the complexes, $Co(HL)_2$ exhibited a crystalline structure, while the others were semi-amorphous, all showing stability up to 500°C. In-vitro anticancer screening against breast (MDA-MB-231, MDA-MB-468) and cervical (HeLa) cancer cell lines revealed significant cytotoxicity, with $Co(HL)_2$ showing the highest potency (IC_{50}: 23.19–25.67 µM) and low toxicity towards normal kidney cells (HEK-293). Computational docking and 100 ns molecular-dynamics simulations demonstrated strong binding affinity and conformational stability of $Co(HL)_2$ within the ATP-binding site of Janus kinase 2 (JAK2), implicating a possible JAK2-targeted apoptotic pathway. These findings highlight the potential of $Co(HL)_2$ Schiff base complex as a promising candidate for targeted anticancer therapy.

Keywords: transition metal complexes; breast cancer; apoptosis; proliferation; colony formation assay.

1. Introduction

Cancer is a complex, multistage progressive disease characterized by the unregulated proliferation of a group of cells, typically triggered by critical mutations within the genetic material of normal cells [1]. Genes that govern cellular proliferation, reproduction, and the cell cycle undergo mutations, thereby converting normal cells into malignant entities. These aberrant cells bypass cellular checkpoints, elude apoptosis, proliferate extensively, increase their biomass, and initiate invasion into adjacent and accessible tissues [2]. The malignant condition affects nearly all bodily systems, organs, and tissues, except for non-living cells such as hair and nails. It is consistently identified in individuals across all age groups. Following its initial invasion of a specific organ or system, the disease subsequently spreads to other parts of the body. There exists a considerable array of over 270 distinct cancer types, many of which exhibit a pronounced tendency to resist chemotherapeutic interventions, resulting in a recurrence following an initial therapeutic response [3].

Breast cancer remains the most prevalent malignancy diagnosed among women across the globe, with incidence rates largely unaffected by regional economic disparities [4]. Significant strides in the molecular characterization and clinical classification, established by the American Society of Clinical Oncology (ASCO) guidelines, have identified a diverse spectrum of biological subtypes - luminal A, luminal B, HER2-enriched, claudin-low, and basal-like - each exhibiting distinct metastatic behaviors, prognostic outcomes [5,6].

Patients diagnosed with luminal subtypes of breast carcinoma often exhibit relapses in bone tissues; conversely, breast carcinomas classified as basal subtypes tend to metastasize to pulmonary and cerebral sites, with statistical significance not achieved in cases involving hepatic relapses. Breast tumor subtypes can be classified based on immunohistochemical (IHC) markers or gene expression profiling. Generally, the conventional prognostic and predictive indicators pertinent to breast cancer disease encompass the status of the human epidermal growth factor receptor 2 (HER2), progesterone receptor (PR), estrogen receptor (ER), and proliferation marker (Ki-67) [7].

Therapeutic options for breast cancer encompass surgical intervention, chemotherapy, radiotherapy, and hormonal therapy, which are dependent upon the disease stage, as well as histopathological and molecular subtype [8]. Mortality disparity persists, with poorer survival rates in low- and middle-income countries compared to high-income regions [9]. Global incidence has risen sharply from 0.6 million cases in 1980 to over 1.6 million by 2010, and projections estimate nearly 3.2 million cases annually by 2030 [10]. Notwithstanding significant advancements in oncological research, breast cancer persists as a prominent health concern and constitutes a primary focus within biomedical research [11].

Despite recent advancements in cancer therapies, the current evidence-based medicine indicates that progress against breast cancer over the preceding decade has been gradual, translating to only a few months of extended survival in metastatic conditions. This limited success primarily arises from intrinsic and acquired drug resistance, narrow therapeutic indices, and tumor heterogeneity, all of which restrict the long-term efficacy of existing chemotherapeutic regimens. Consequently, there is an urgent need to develop new classes of metallopharmaceuticals that can selectively target cancer pathways while minimizing systemic toxicity [12].

In this regard, inorganic medicinal chemistry has emerged as a transformative field, providing molecular frameworks that leverage the extensive redox properties, diverse coordination geometries, and distinctive ligand-exchange kinetics of transition metals to facilitate targeted cytotoxic effects [13]. The elucidation of the DNA-interacting and apoptosis-promoting properties of platinum-derived compounds, including cisplatin, carboplatin, and oxaliplatin, has catalyzed the systematic development of non-platinum metal complexes aimed at overcoming their inherent challenges, including drug resistance and nephrotoxicity [14].

Schiff base metal complexes signify a notably versatile class of coordination compounds, wherein the imine (–C=N–) linkage functions as a dynamic and electron-rich coordination site. Their modifiable donor atoms, structural versatility, and ability to stabilize metals across various oxidation states facilitate precise control of electronic distribution, lipophilicity, and biomolecular interactions [15]. Phenolic frameworks are particularly appealing for anticancer applications due to their ability to engage in both covalent and noncovalent interactions, thereby enhancing cellular permeability and promoting apoptotic signaling via oxidative stress or protein inhibition pathways. Their intrinsic chelating proficiency also confers enhanced thermodynamic stability and kinetic inertness, thereby reducing off-target toxicity compared with traditional platinum-based pharmacological agents [16].

The current work extends this conceptual framework by presenting a novel dopamine-derived bidentate Schiff base incorporating a 1,4-benzodioxane moiety, specifically designed to modulate the electronic density at the phenolic coordination sites. This structural modification significantly improves the metal–ligand interaction and has the potential to enhance biological affinity through π–π stacking and hydrogen-bonding interactions with target proteins. Moreover, by integrating *in vitro* cytotoxicity assessments with *in silico* molecular docking analyses and 100 ns molecular dynamics simulations, the research offers a comprehensive experimental–computational insight into how coordination geometry affects the inhibition of the JAK2 kinase pathway—a mechanistic relationship that has been infrequently investigated within the realm of Schiff base chemistry.

2. Materials and Methods

2.1. Materials.

All chemicals, solvents, and reagents employed in this study were of analytical grade and were used as received without any additional purification. Dopamine hydrochloride (≥ 98%, Signma-Aldrich), 1,4-benzodioxane-6-carboxaldehyde (≥ 98%, Merck India), triethylamine (TEA) (≥ 99%, SD Fine Chemicals), and metal salts ((≥ 98%, Merck India) were used for synthesis. The solvents used were HPLC and AR grade. FT-IR spectra were obtained using an Agilent Cary 630 FT-IR spectrophotometer. Powder X-ray diffraction (P-XRD) data were collected using an AXRD benchtop powder diffractometer. Thermogravimetric analysis (TGA) was conducted under a nitrogen atmosphere using a TGA 4000 instrument.

2.2. Methods.

2.2.1. Synthesis of Schiff base ligand (HL) containing benzodioxane.

The Ligand (HL) was synthesised by refluxing a 1:1 molar mixture of dopamine hydrochloride and 1,4-benzodioxane-6-carboxaldehyde (1 mmol each) in ethanol (25 ml), in the presence of triethylamine (TEA, 0.1ml) as a base. The reaction was carried out at 60°C for 24 h. The resulting product was filtered, washed with ethanol, and dried under vacuum at 50°C (Scheme 1).

Yield: 89%; Color: Black Color solid; Decomp. Temp. (°C): 226-227.

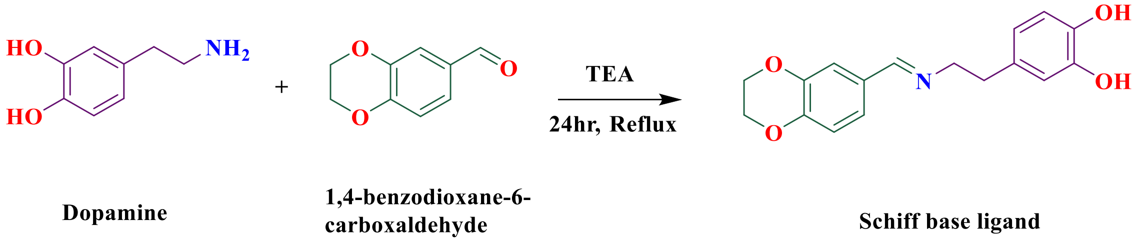

Scheme 1. Synthetic route for the synthesis of metal complexes.

2.2.2. Synthesis of metal complexes M(HL)$_2$.

A solution of Ligand (HL) (2mmol) in DMSO (15 ml) was prepared and mixed with an aqueous solution (10 ml) of the corresponding metal salt [$CuCl_2$, $CoCl_2$, $NiCl_2$, $ZnCl_2$] (1 mmol) in a 2:1 ratio. The reaction mixture was subjected to microwave irradiation for 25-30 min, during which a distinct color change was observed. The solid product obtained was separated by filtration, rinsed with distilled water, and dried at 40 °C in a hot-air oven (Scheme 2).

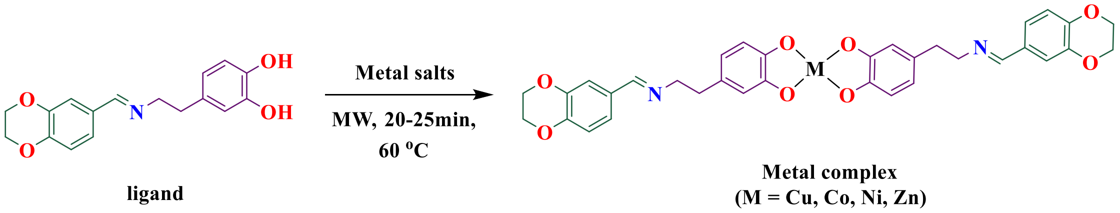

Scheme 2. Synthetic route for the synthesis of metal complexes.

2.2.3. Cell lines and culture conditions.

Human cervical cancer (HeLa) and breast cancer cell lines (MDA-MB-231 and MDA-MB-468) were obtained from the National Centre for Cell Sciences (NCCS), Pune, India. Prof. Sathees C. Raghavan generously provided normal human embryonic kidney (HEK-293) cells from the Department of Biochemistry at the Indian Institute of Science (IISc), Bengaluru. The cells were cultured in DMEM (low glucose), RPMI 1640, and DMEM (high glucose) media, respectively, supplemented with 2 mM L-glutamine (Thermo Fisher Scientific, Waltham, MA, USA) and 10% fetal bovine serum (FBS; Gibco, Grand Island, NY, USA). All cell lines were maintained in a humidified incubator at 37°C, with or without 5% CO_2 as per their specific growth requirements [17]. Cells in the exponential growth phase (70–80 % confluence) were used for all experiments, and mycoplasma contamination was routinely checked.

2.2.4. MTT and trypan blue dye exclusion assay.

The cytotoxic activity of the synthesized complexes was assessed by the MTT [3-(4,5-dimethylthiazol-2-yl)-2,5-diphenyltetrazolium bromide] assay [18], using DMSO ($\leq 0.1\%$ v/v) as the vehicle control. HeLa, MDA-MB-231, MDA-MB-468, and HEK-293 cells were seeded in 96-well plates at a density of 7,500 cells per well in 200 µL of complete growth medium and incubated for a duration of 24 hours to facilitate cellular adherence. The cells were subsequently treated with increasing concentrations (5, 10, 25, 50, 75, and 100 µM) of each complex for 48 and 72 hours. Following treatment, 20 µL of MTT reagent (5 mg mL^{-1} in PBS) was introduced to each well and incubated for 4 hours at 37°C. Subsequently, the medium was discarded, and 150 µL of DMSO was incorporated to ensure the complete dissolution of the formazan crystals. Absorbance measurements were conducted at 570 nm utilizing a Tecan Infinite 200 PRO microplate reader (Tecan Instruments, Switzerland). Data were acquired with Magellan software and analyzed using GraphPad Software 9.0 (GraphPad Software Inc., San Diego, CA, USA).

All experiments were performed in triplicate (n = 3) and repeated independently at least twice. The half-maximal inhibitory concentration (IC_{50}) values were determined by fitting the data to a four-parameter logistic regression model. The results were expressed as mean ± standard deviation (SD), and statistical significance was evaluated using one-way ANOVA with Tukey's post hoc multiple-comparison test, with $p < 0.05$ considered statistically significant.

The trypan blue dye exclusion assay [19] was also employed to evaluate the impact of the synthesized complexes on cellular viability under identical experimental parameters (5–100 µM, 48–72 h). Cells were harvested, mixed in a 1:1 ratio with 0.4% Trypan Blue solution, and counted using a hemocytometer under an inverted microscope (Olympus CKX53). DMSO-treated cells served as vehicle controls. The percentage of viable cells was calculated using the formula:

$$\text{Cell viability (\%)} = \frac{\text{Number of unstained cells}}{\text{Total number of cells}} \times 100 \qquad (1)$$

Data are represented as mean ± SD derived from three independent experiments (n = 3) and graphically illustrated as histograms with error bars to denote variability.

2.2.5. Apoptotic analysis by Hoechst/PI staining.

Apoptotic nuclear morphology was assessed by dual staining with Hoechst 33342 and propidium iodide (PI) according to the protocol established by [20], with slight modifications. HeLa, MDA-MB-231, and MDA-MB-468 cell lines were cultured in 6-well plates at a density of 1×10^5 cells per well, with overnight adherence. The next day, the cells were treated with the test complex at 25 µM for 48 hours, with DMSO (≤ 0.1%, v/v) as the vehicle control. Following the incubation period, cells were washed twice with phosphate-buffered saline (PBS) and subsequently stained with Hoechst 33342 (5 µg mL^{-1}) and PI (2 µg mL^{-1}) for 10 minutes in the dark at room temperature. The stained nuclei were promptly analyzed under an Olympus CKX53 fluorescence microscope utilizing DAPI (for Hoechst) and Texas Red (for PI) filter sets to facilitate the visualization of chromatin condensation, nuclear fragmentation, and membrane integrity. The quantification of apoptotic and necrotic cells was conducted from a minimum of 5 randomly selected microscopic fields per well, with data expressed as mean ± standard deviation (SD) derived from 3 independent experimental replicates (n = 3).

2.2.6. Colony formation assay.

The clonogenic potential of cancer cells following treatment with the synthesized metal complexes was assessed using the colony-forming assay, as described in [21], with minor modifications. Cells (2,000 per well) were inoculated in 6-well plates and permitted to adhere overnight under standardized culture conditions. The following day, cells were subjected to increasing concentrations (5, 10, 25, and 50 µM) of the $Co(HL)_2$ and $Zn(HL)_2$ complexes for 14 days. The culture medium was systematically replaced every 3 days with newly prepared treatment solutions to ensure uniform drug exposure.

After incubation, the colonies were rinsed with phosphate-buffered saline (PBS), fixed in a methanol–acetic acid solution (7:1, v/v) for 10 minutes, and subsequently stained with 0.5% (w/v) crystal violet for 30 minutes at room temperature. The plates were washed with distilled water to remove excess dye, then air-dried. Colonies containing at least 50 cells were manually counted, and images were analyzed using ImageJ (NIH, USA) for quantitative assessment. The results were articulated as mean ± standard deviation (SD) derived from three independent experiments (n = 3).

2.2.7. Annexin V- FITC/PI staining.

The apoptotic progression induced by the synthesized metal complexes was further assessed using Annexin V-FITC/PI dual staining (Roche Apoptosis Detection Kit) according to the manufacturer's protocols. Briefly, cells were cultured in 6-well plates and subjected to treatment with 25 µM of $Co(HL)_2$ or $Zn(HL)_2$ for a duration of 24 hours with DMSO ($\leq 0.1\%$, v/v) functioning as vehicle controls. After treatment, cells were collected, washed twice with cold phosphate-buffered saline (PBS), and resuspended in 1× binding buffer at a density of approximately 1×10^5 cells per 100 µL. Thereafter, 5 µL of Annexin V-FITC and 10 µL of propidium iodide (PI) were added to each sample, followed by a 15-minute incubation at room temperature in the dark. Upon completion of the staining process, 400 µL of binding buffer was introduced, and the cells were immediately examined under an Olympus CKX53 inverted fluorescence microscope employing FITC (green) and Texas Red (red) filter sets. Early- and late-apoptotic populations, as well as necrotic cells, were identified by fluorescence characteristics and quantified by counting at least 500 cells per field across three independent experiments (n = 3) [18].

2.2.8. *In-silico* validation-docking studies.

In view of the promising *in vitro* anticancer activity—particularly the pronounced inhibitory effect observed with the $Co(HL)_2$ complex—molecular docking studies were performed to explore the potential binding interactions of the synthesized complexes with a cancer-associated target protein. The three-dimensional structure of the selected protein was retrieved from the RCSB Protein Data Bank using the PDB ID: 3KRR. Docking simulations were performed using AutoDock Tools (ADT) version 1.5.6 with default parameters for grid generation and docking protocol setup. The receptor structure was prepared by eliminating co-crystallized ligands and water molecules, followed by the incorporation of hydrogen atoms. Non-polar hydrogens were merged with their respective parent atoms, and partial charges were assigned using the Kollman method. Subsequently, the receptor was saved in PDBQT format. Ligand structures were similarly prepared by defining rotatable bonds and assigning Gasteiger charges prior to their conversion to PDBQT format [22]. Molecular docking was performed to ascertain the most favorable binding pose based on binding energy assessments. The resulting protein–ligand interactions were visualized and analyzed utilizing Biovia Discovery Studio 2019 [23].

2.2.9. Molecular dynamic simulation.

Molecular dynamics (MD) simulations of the JAK2 protein-ligand complex were performed using GROMACS software. The simulations followed a standard protocol for protein–ligand systems, employing the GROMOS96 force field to generate the protein topology. A cubic simulation box was constructed around the complex, solvated with water molecules, and neutralized by adding appropriate counter-ions. The system underwent energy minimization, followed by equilibration in the NVT and NPT ensembles at 300 K. A production MD run was then carried out for 100 ns. Post-simulation analyses included root-mean-square deviation (RMSD), root-mean-squarefluctuation (RMSF), radius of gyration (Rg), solvent-accessible surface area (SASA), number of hydrogen bonds, and Gibbs free energy landscape (FEL).

3. Results and Discussion

3.1. Chemistry.

The Schiff base ligand, along with its bivalent transition metal complexes $Cu(HL)_2$, $Co(HL)_2$, $Ni(HL)_2$, and $Zn(HL)_2$, formed through the condensation of Dopamine Hydrochloride with 1,4-benzodioxane-6-carboxaldehyde in ethanol, yielded an analytical outcome that aligns well with the proposed formulas of the chelates. The acquired physical-analytical data clearly indicate a 1:2 stoichiometric ratio of metal to ligand for all complex systems, which aligns with the proposed structural formulas and thereby validates the hypothesized mononuclear configuration for the metal complexes. Table 1 presents the structural and chemical data of the synthesized ligand and its complexes.

Table 1. Physical and chemical data of ligand and complexes.

Sl no.	Molecular formula	Structure	Molecular weight	Yield
1	$C_{17}H_{17}NO_4$	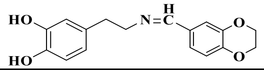	299.32	90
2	$Cu(C_{17}H_{17}NO_4)_2$	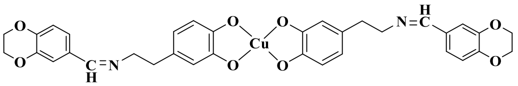	658.17	72
3	$Co(C_{17}H_{17}NO_4)_2$	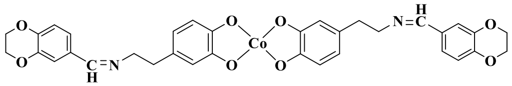	668.59	85
4	$Ni(C_{17}H_{17}NO_4)_2$	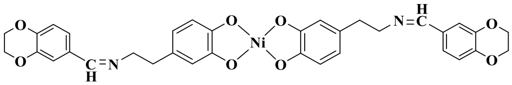	676.35	78
5	$Zn(C_{17}H_{17}NO_4)_2$	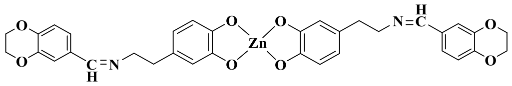	678.45	81

3.2. Characterization.

3.2.1. Molecular dynamic simulation.

The principal FT-IR spectral characteristics of the Schiff base ligand (HL) and its corresponding metal complexes are presented in Table 2 and depicted in Figure 1. In the spectrum of HL, a sharp band at 1607 cm^{-1} is assigned to the azomethine (–CH=N–) stretching vibration, confirming successful Schiff base formation. This band shifts marginally to 1605–1610 cm^{-1} in the metal complexes, indicating slight electronic perturbation upon complexation, though suggesting non-involvement of the imine nitrogen in direct coordination. A prominent band observed at 3197 cm^{-1} in the free ligand, corresponding to the phenolic –OH stretch, disappears in all metal complexes. This observation strongly supports deprotonation of the hydroxyl group and subsequent coordination via the phenolic oxygen.

Table 2. Physical and chemical data of ligand and complexes.

Compound	ν(OH)	ν(C=N)	(C-O)	ν(C-N)	M-O
HL	3197	1607	1187	1270	-
$[Cu(HL)_2]$	-	1607	1113	1274	640
$[Ni(HL)_2]$	-	1607	1119	1278	652
$[Co(HL)_2]$	-	1610	1119	1275	636
$[Zn(HL)_2]$	-	1605	1119	1275	645

Additionally, the ν(C–O) band at 1187 cm^{-1} in HL undergoes a red shift to 1113–1119 cm^{-1} in the metal complexes, further validating metal–oxygen coordination. The emergence of new bands in the 636–652 cm^{-1} range, attributed to ν(M–O) stretching vibrations, provides additional evidence for complex formation via phenolic-oxygen coordination. Collectively, the spectral changes confirm the bidentate binding mode of HL via the phenolic oxygen atoms π-back-donation [24].

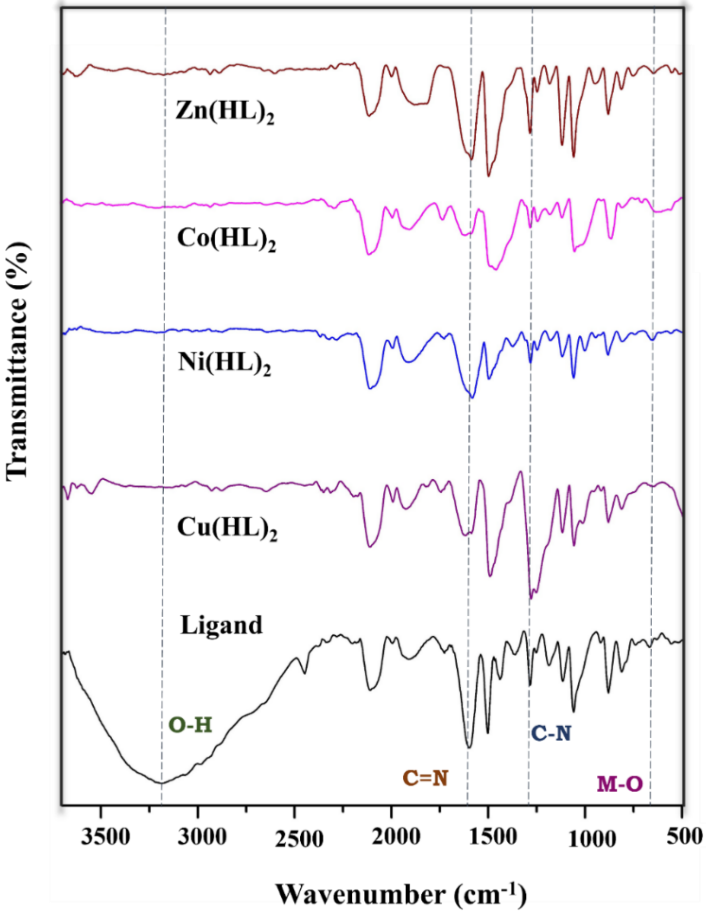

Figure 1. FT-IR spectra of the free Schiff-base ligand (HL) and its corresponding metal complexes..

3.2.2. XRD.

The HL and its metal complexes were analyzed utilizing powder X-ray diffraction (PXRD) within a 2θ range of 10° to 80°. Among the complexes examined (Figure 2), only the Co(HL)$_2$ complex exhibited sharp, well-defined peaks, confirming its crystalline nature. In contrast, the Cu(HL)$_2$, Ni(HL)$_2$, and Zn(HL)$_2$ complexes showed broad and diffuse peaks, suggesting a semi-amorphous or poorly crystalline state, consistent with partial ordering. The interplanar spacing (d) was determined using Bragg's law, $n\lambda = 2d\sin\theta$. The calculated d-spacing values, along with their relative intensities compared to the most intense diffraction peak for each complex, are presented in Tables S1–S4. Initially, unit cell parameters were calculated assuming cubic symmetry by indexing all major diffraction peaks and assigning corresponding h2 + k2 + l2 values. A close correlation was observed between the experimentally determined and theoretically calculated d-spacing values, indicating reliable indexing. However, the appearance of a forbidden reflection with index number 7 in the patterns of Ni(HL)$_2$ and Co(HL)$_2$ complexes indicates that these may not follow a purely cubic system. Instead, this may suggest a non-cubic crystal system, such as tetragonal or hexagonal [25]. To further investigate crystallinity, the crystallite size (D_{XRD}) of the complexes was computed employing Scherrer's formula [26,27]. The average crystallite sizes for the Cu(HL)$_2$, Co(HL)$_2$, Ni(HL)$_2$, and Zn(HL)$_2$ complexes were determined to be 5.93, 165.27, 7.56, and 8.90

nm, respectively. These findings offer valuable insights into the structural and morphological characteristics of the synthesized complexes.

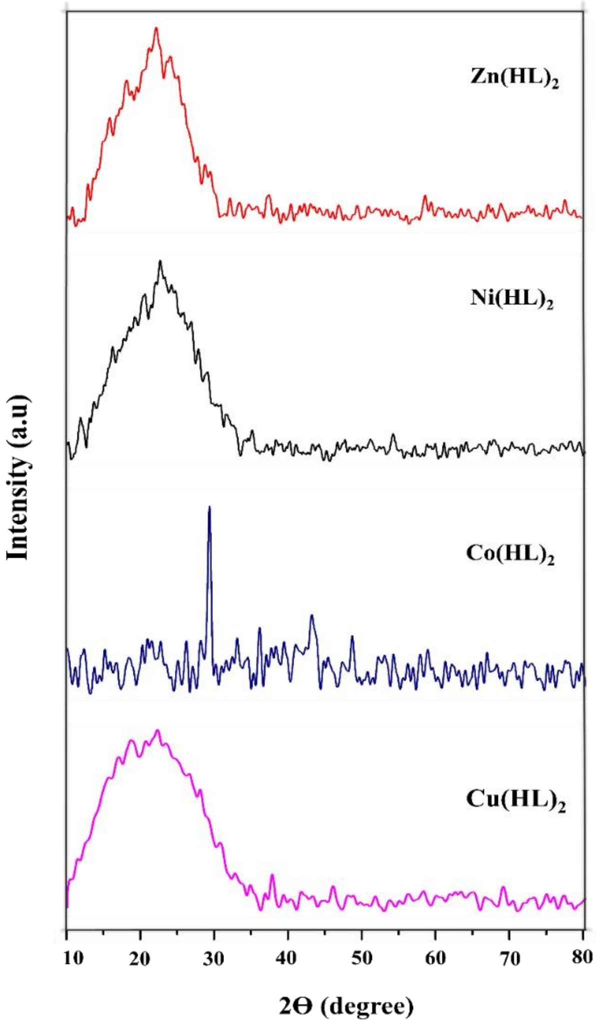

Figure 2. PXRD patterns of $Cu(HL)_2$, $Co(HL)_2$, $Ni(HL)_2$, and $Zn(HL)_2$ recorded in the 2θ range 10°–80° using Cu Kα radiation (λ = 1.5406 Å; scan rate = 2° min^{-1}).

3.2.3. Thermal analysis.

The thermal stability of all synthesised complexes was assessed using thermogravimetric (TG) analysis under N_2 atmosphere. The TG curve and corresponding degradation steps are shown in Figure 3 and Table 3. The thermal data acquired provide strong evidence in favor of the proposed stoichiometry of the compounds and indicate that the thermal degradation mechanism of HL occurs in two distinct phases. The initial phase occurs at 84°C, with a weight loss of 6-8%, corresponding to the loss of H_2O. The subsequent phase occurs at 621°C, yielding 90% weight loss and the expulsion of the HL, resulting in the residue product C. The thermal decomposition patterns of the complexes are similar, showing three degradation stages, except for the Zn(HL)2 complex, which exhibits a two-step degradation process. The first decomposition phase is invariably accompanied by the loss of hydration water across all complexes. For the $Cu(HL)_2$, $Co(HL)_2$, and $Ni(HL)_2$ complexes, the second decomposition stage transpires within the temperature range of 358 – 398°C, resulting in the loss of $C_8H_8O_2$ from the HL. The third decomposition stage occurs within the temperature interval of 496 - 682°C, leading to the loss of the remaining ligand portion, yielding CuO+2C, CoO+3C, and Ni, respectively, as byproduct residues. In the case of $Zn(HL)_2$, the second decomposition stage occurs at 609°C, resulting in the degradation of HL to yield ZnO and 3C. For all complexes investigated, the observed weight loss corresponding to each decomposition phase agrees with the measured weight loss. The proposed thermal decomposition pathways of HL and its metal complexes are based on reasonable assumptions derived from the experimental observations [28].

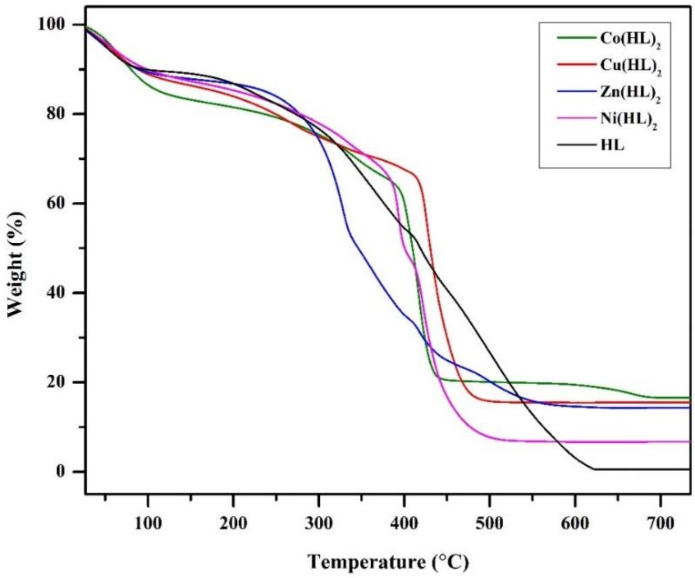

Figure 3. TGA curves of HL and its metal complexes [$Cu(HL)_2$, $Ni(HL)_2$, $Co(HL)_2$, $Zn(HL)_2$] recorded under N_2 atmosphere (25–800°C; heating rate 10°C min^{-1}).

Table 3. Thermal analysis data of the synthesized metal complexes.

Compound	**Decomposition**	**T_{max}(°C)**	**Weight loss (%)**		**Lost species**
			Calculated	**Found**	
HL	1st step	84	6.02	8.66	H_2O
	2nd step	621	89.97	89.79	Organic ligand
	Total loss		95.99	98.45	
	Residue		4.011	1.54	
$[Cu(HL)_2]$	1st step	103	10.95	10.55	HCl + 2.H_2O
	2nd step	398	20.54	20.53	$C_8H_8O_2$
	3rd step	496	53.04	52.46	Organic ligand
	Total loss		84.53	83.54	
	Residue		15.60	16.26	CuO+2C
$[Co(HL)_2]$	1st step	89	11.02	11.20	HCl + 2.H_2O
	2nd step	358	20.60	20.05	$C_8H_8O_2$
	3rd step	682	51.40	52.07	ligand
	Total loss		83.02	83.32	
	Residue		16.97	16.68	CoO+3C
$[Ni(HL)_2]$	1st step	98	8.28	9.06	HCl + H_2O
	2nd step	371	20.71	21.78	$C_8H_8O_2$
	3rd step	518	62.04	61.4	ligand
	Total loss		91.03	92.24	
	Residue		8.99	7.76	Ni
$[Zn(HL)_2]$	1st step	106	10.91	10.14	HCl + 2.H_2O
	2nd step	609	73.74	74.09	ligand
	Total loss		84.65	84.23	
	Residue		15.36	15.77	Zn + 3C

3.3. Anticancer.

3.3.1. Metal complexes inhibit cancer cell proliferation.

The *in vitro* cytotoxic potential of the synthesized metal complexes was evaluated against human cervical adenocarcinoma (HeLa), human breast cancer (MDA-MB-231 and MDA-MB-468), and normal human embryonic kidney (HEK-293) cell lines using the MTT and trypan blue exclusion assays. Among the tested complexes, both Co(HL)$_2$ and Zn(HL)$_2$ demonstrated minimal cytotoxicity toward normal HEK-293 cells, with IC$_{50}$ values exceeding 100 µM, indicating selective toxicity toward cancer cells (Figure 4; Figure S1).

The Co(HL)$_2$ complex emerged as the most efficacious agent, exhibiting significant dose- and time-dependent cytotoxic effects across all neoplastic models. It demonstrated the greatest potency against MDA-MB-468 cells, with an IC$_{50}$ value of 23.19 ± 0.24 µM, followed by HeLa (22.53 ± 0.54 µM) and MDA-MB-231 (25.67 ± 0.16 µM) cells (Figure 4). In contrast, the Zn(HL)$_2$ complex exhibited moderate yet consistent cytotoxic activity across all evaluated cancer cell lines, with IC$_{50}$ values varying from 28.44 ± 0.32 µM to 40.32 ± 0.28 µM (Figure S1). Both complexes demonstrated minimal cytotoxicity in normal HEK-293 cells, with IC$_{50}$ values exceeding 100 µM, thereby affirming their selective toxicity towards malignant cells. The remaining synthesized complexes containing Cu(HL)$_2$ and Ni(HL)$_2$ metal ions did not demonstrate a reduction in viability in the tested cancer cell lines. The IC$_{50}$ values for all complexes are presented in Table 4.

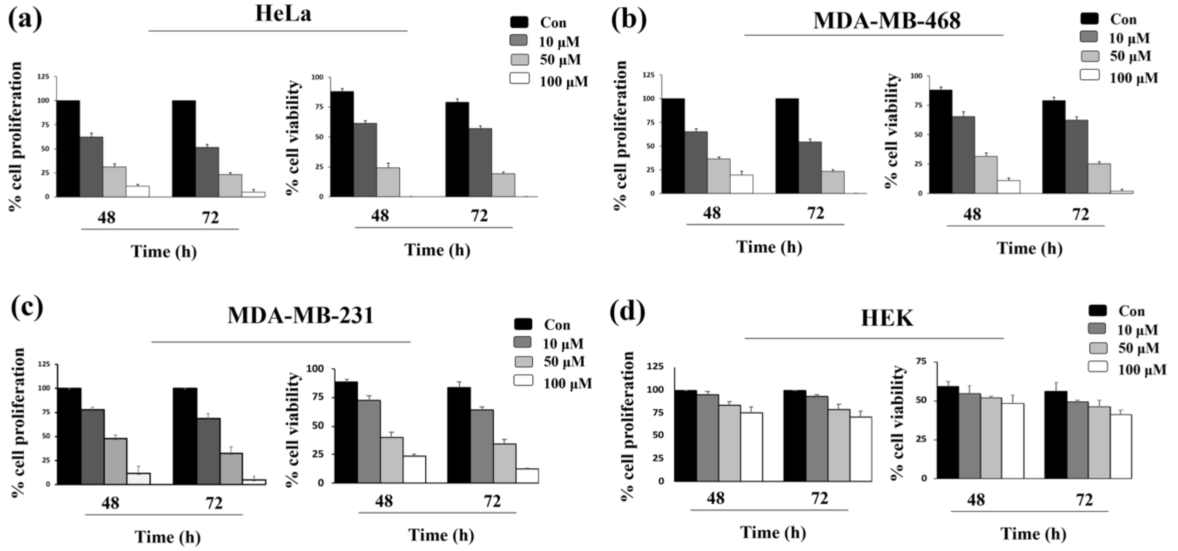

Figure 4. Effect of Co(HL)$_2$ complex on cell proliferation and viability: **(a)** HeLa cells treated with Co(HL)$_2$ (10, 50 and 100 µM) for 48 and 72 h, assessed by MTT and Trypan Blue assays; **(b)** MDA-MB-468 cells treated under identical conditions showing dose- and time-dependent reduction in viability; **(c)** MDA-MB-231 cells exhibiting decreased proliferation and viability with increasing Co(HL)$_2$ concentrations; **(d)** Normal HEK-293 cells showing minimal cytotoxicity even at higher Co(HL)$_2$ doses, confirming selective toxicity toward cancer cells. Data represent mean ± SD from three independent experiments; DMSO-treated cells served as vehicle controls.

Table 4. IC$_{50}$ values of metal complexes against cancer and normal cell lines.

Cell lines	**IC$_{50}$ (µM)**			
	[Cu(HL)$_2$]	**[Co(HL)$_2$]**	**[Ni(HL)$_2$]**	**[Zn(HL)$_2$]**
HeLa	22.53 ± 0.54	40.32 ± 0.28	>100	>100
MDA-MB-468	**23.19 ± 0.24**	34.76 ± 0.35	>100	>100
MDA-MB-231	25.67 ± 0.16	**28.44 ± 0.32**	>100	>100
HEK	> 100	> 100	>100	>100

3.3.2. Metal complexes potentiate apoptosis in breast cancer cells.

Anticancer agents exert their therapeutic effects by inhibiting the proliferation of malignant cells and promoting programmed cell death (apoptosis), primarily by modulating regulatory proteins that are integral to essential signaling pathways. To elucidate the mechanism of cell death induced by the synthesized Co(HL)$_2$ and Zn(HL)$_2$ complexes, the Hoechst 33342/propidium iodide (PI) dual staining assay was employed. As depicted in Figure

5, MDA-MB-468 cells treated with the $Co(HL)_2$ complex (25 µM) exhibited distinct morphological changes characteristic of apoptosis, including chromatin condensation and nuclear fragmentation (Hoechst-positive), coupled with red PI fluorescence indicating late apoptotic cells. Conversely, DMSO-treated control cells displayed intact, uniformly stained nuclei with minimal PI uptake, thereby confirming the absence of apoptosis.

Similarly, Figure S2 illustrates the apoptotic effects of the $Zn(HL)_2$ complex on MDA-MB-231 cells, where treatment (25 µM) resulted in significant nuclear condensation and an increase in PI-positive staining relative to the control group. Quantitative analysis further revealed that the $Co(HL)_2$ complex induced a higher percentage of apoptotic cells at lower concentrations than the $Zn(HL)_2$ complex (Figure 5b; Figure S2b).

Collectively, these observations, in conjunction with prior cytotoxicity findings, suggest that both $Co(HL)_2$ and $Zn(HL)_2$ complexes induce apoptosis via a mitochondrial-mediated intrinsic pathway in MDA-MB-468 and MDA-MB-231 breast cancer cells. The enhanced apoptotic response provoked by the $Co(HL)_2$ complex indicates its superior potential as a selective anticancer candidate when compared to the $Zn(HL)_2$ complex.

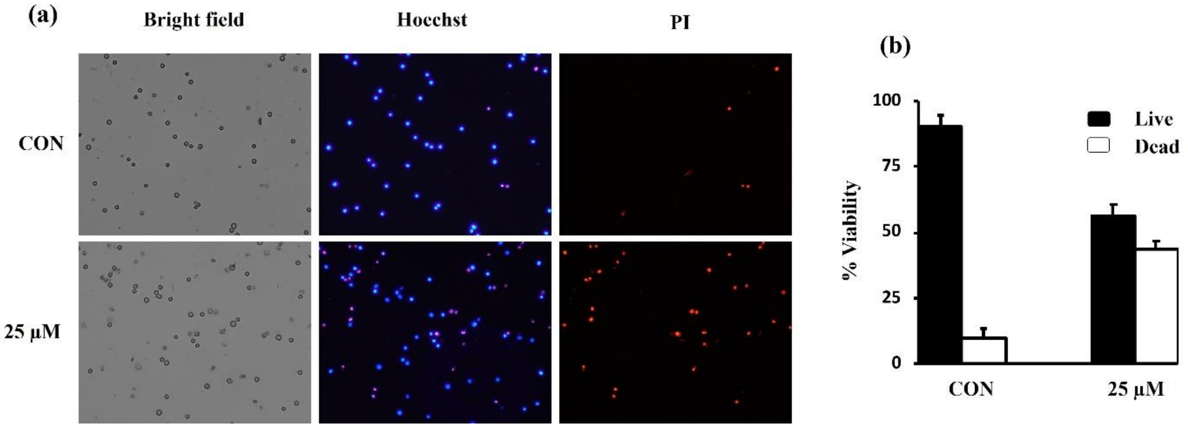

Figure 5. Induction of apoptosis in MDA-MB-468 cells by $Co(HL)_2$ complex: **(a)** Bright-field, Hoechst, and PI images of control and 25 µM $Co(HL)_2$-treated cells after 24 h; **(b)** Percentage of live and dead cells quantified from Hoechst/PI staining (mean ± SD, n = 3; ≥500 cells counted).

3.3.3. Metal complexes decline colony formation and induce apoptosis.

The clonogenic assay, which assesses the capacity of an individual cell to persist and generate a colony, was utilized to ascertain the long-term antiproliferative efficacy of the synthesized $Co(HL)_2$ and $Zn(HL)_2$ complexes against triple-negative breast cancer (TNBC) cell lines MDA-MB-468 and MDA-MB-231, respectively [29]. Cells were exposed to various concentrations (5, 10, 25, and 50 µM) of each complex for 14 days. Both complexes demonstrated significant inhibition of colony formation in a dose-dependent manner, with nearly complete suppression of clonogenic growth at 50 µM (Figure 6; Figure S3). Notably, the $Co(HL)_2$ complex exhibited a more pronounced inhibitory effect on MDA-MB-468 cells, achieving significant colony reduction even at a concentration of 25 µM. In contrast, the $Zn(HL)_2$ complex necessitated marginally elevated concentrations to produce comparable inhibition in MDA-MB-231 cells. Despite these variations, both TNBC cell lines showed substantial sensitivity to their respective metal complexes.

The pro-apoptotic activity of the $Co(HL)_2$ and $Zn(HL)_2$ complexes was further evaluated through the application of Annexin V-FITC/PI dual staining. MDA-MB-468 cells were treated with 25 µM $Co(HL)_2$, while MDA-MB-231 cells were exposed to 30 µM $Zn(HL)_2$ for a period of 24 hours, with DMSO (≤ 0.1%) serving as the vehicle control. Fluorescence microscopy revealed distinctive staining patterns indicative of apoptosis: early apoptotic cells showed green fluorescence (Annexin V-positive), whereas late apoptotic cells showed a combination of green and red fluorescence (Annexin V + PI-positive). Importantly, no necrotic cells (PI-positive only) were identified, thereby confirming that both $Co(HL)_2$ and $Zn(HL)_2$ complexes induced apoptotic rather than necrotic cell death in TNBC models (Figure 6; Figure S3).

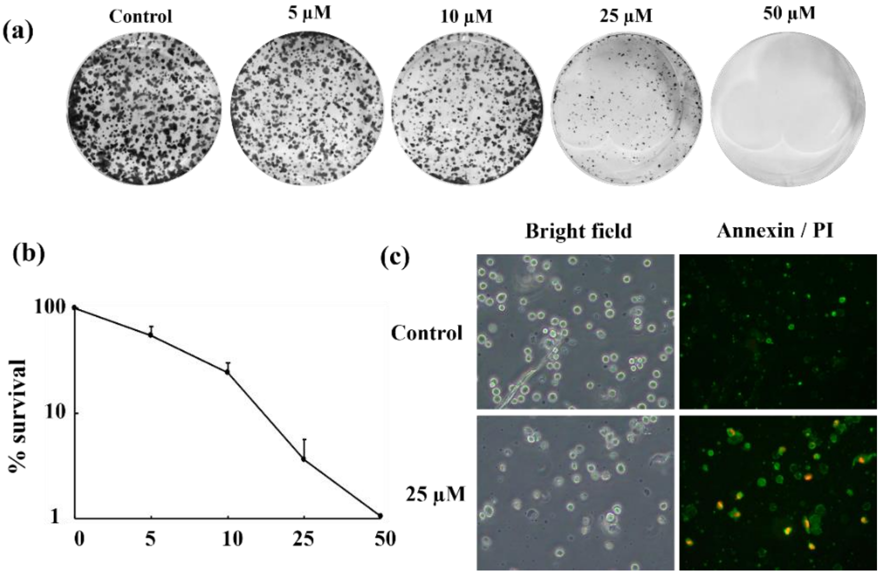

Figure 6. Effect of $Co(HL)_2$ complex on colony formation and apoptosis: MDA-MB-468 cells were treated with different concentrations of $Co(HL)_2$ complex and subjected to survival and apoptotic analysis: **(a)** Crystal violet-stained colonies; **(b)** Percentage survival graph; **(c)** Annexin PI-stained cells.

3.3.4. Predictive mechanistic pathway by *in-silico* validation.

Breast Cancer ranks among the most prevalent malignant tumors globally, distinguished by a pronounced risk of metastasis and recurrence. Despite significant progress in medical technology, current BC treatments result in inescapable adverse effects such as fatigue, nausea, vomiting, and osteoporosis-related complications [30]. Consequently, the urgent necessity for the development of low-toxicity drugs with minimal adverse effects is clearly established. Natural Dietary compounds, especially phenolic-rich fruits such as pomegranate, mangosteen, and citrus, have shown significant cytotoxic effects against Breast Cancer cells [31]. In this study, we observed that HL and its $Co(HL)_2$ and $Zn(HL)_2$ complexes exhibit potential anticancer activity, effectively inhibiting the proliferation of BC cells [32]. The uncontrolled proliferation of tumor cells is a major contributor to tumor initiation and progression [33]. Apoptosis, or programmed cell death, functions as an essential mechanism for arresting tumor development [34].

The $Co(HL)_2$ and $Zn(HL)_2$ complexes demonstrated significant cytotoxic effects against MDA-MB-468 and MDA-MB-231 breast cancer cell lines, with IC_{50} values of 23.19 ± 0.24 μM and 25.67 ± 0.16 μM for MDA-MB-468, and 34.76 ± 0.35 μM and 28.44 ± 0.32 μM for MDA-MB-231, measured at 48 and 72 hours, respectively. Notably, both complexes exhibited minimal cytotoxicity toward the HEK-293 regular kidney cell line, suggesting a degree of selectivity for cancerous cells over normal cells [35].

STAT proteins are integral to tumorigenesis across a variety of malignancies. PIAS3, a key cellular inhibitor of STAT3, regulates the activity of DNA-binding transcription factors [36]. Following activation, JAKs phosphorylate STAT proteins, which leads to dimerization and subsequent nuclear translocation. Within the nucleus, STATs function as transcription factors, governing the expression of genes implicated in cellular proliferation and survival. In oncogenesis, persistent STAT3 activation promotes the expression of oncogenic genes, thereby facilitating enhanced cellular proliferation [35]. The present *in-silico* analyses revealed strong binding affinities of Co(HL)$_2$ (−7.79 kcal/mol) and Zn(HL)$_2$ (−9.52 kcal/mol) for the ATP-binding domain of Janus kinase 2 (JAK2). The Co(HL)$_2$ complex established extensive hydrogen bonding and hydrophobic interactions with JAK2, resulting in a stable ligand–protein complex, as validated by molecular dynamics (MD) simulations. Evaluations of RMSD, radius of gyration (Rg), and Gibbs Free Energy profiles further corroborate a thermodynamically stable and compact structure, indicative of sustained inhibitory potential.

Overall, the findings indicate that the Co(HL)$_2$ and Zn(HL)$_2$ complexes exert potent anti-proliferative effects on MDA-MB-468 and MDA-MB-231 breast cancer cells by inducing mitochondrial-mediated apoptosis. In addition, both complexes exhibit significant anticancer activity by effectively inhibiting the JAK2/STAT3 signaling pathway.

3.4. Molecular docking results.

In this work, we examine the efficacy of complexes as inhibitors of the JAK2 receptor in cancer. The JAK2/STAT3 signaling pathway is a prevalent signaling cascade implicated in various pathologies, including cancer and inflammation, and promotes tumorigenesis, tumor expansion, cancer cell survival, and metastasis of solid tumors. This compelling association of the JAK2/STAT3 pathway with tumorigenesis provides novel therapeutic targets for chemotherapy and facilitates advancements in cancer treatment methodologies [23]. Hence, in the current work, the biological activity of the HL, Co(HL)$_2$, and Zn(HL)$_2$ complexes was analyzed computationally using molecular docking against the JAK2 protein (PDB: 3KKR).

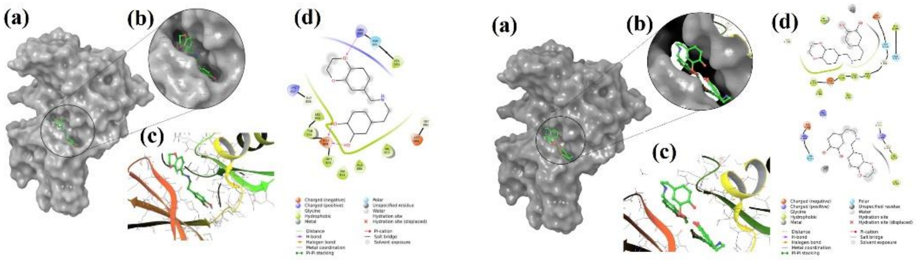

HL

Co(HL)$_2$

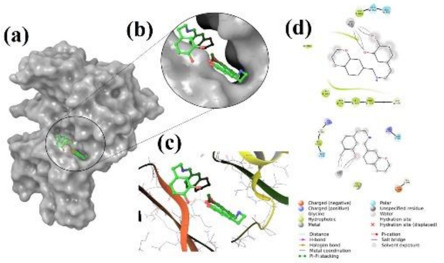

Zn(HL)$_2$

Figure 7. Molecular docking of HL and its Co(HL)$_2$ and Zn(HL)$_2$ complexes: **(a)** 3D surface showing HL and complexes in the active binding pocket of the protein; **(b)** Focused view of the compounds in the active binding pocket; **(c)** Ribbon diagram of the local binding environment, showing key interactions—hydrogen bonds (dashed cyan), π–π stacking (dashed green), and hydrophobic contacts; **(d)** 2D interaction schematic of HL and complexes with 3KRR residues.

The resulting relative binding energy ((kcal/mol) negative energy values) of docked HL, Co(HL)$_2$, and Zn(HL)$_2$, with JAK2 protein were observed to be -6.68, -7.79, and -9.52

kcal/mol, respectively (Table 5). As shown in Figure 7, all compounds bind in the active binding pocket of the protein, thereby resulting in inhibitory effects on the JAK2 protein.

Table 5. Docking results of the ligand and its complexes.

Compound	Free Energy of Binding (kcal/mol)
HL	-6.68
$Cu(HL)_2$	-6.32
$Co(HL)_2$	-7.79
$Ni(HL)_2$	-5.85
$Zn(HL)_2$	-9.52

3.4. Molecular dynamics results.

The molecular dynamics simulation approach is used to investigate the physical movements of protein-ligand conformations, thereby yielding valuable insights into their operational mechanisms. In the present study, Schiff base ligands and their $Co(HL)_2$ complexes, identified through docking analyses as exhibiting the highest binding energies and inhibition constants relative to their respective target proteins, were selected for molecular dynamics simulation to assess the stability and flexibility of these conformations. The stability of the HL and the $Co(HL)_2$ complex in association with the 3KRR protein is analyzed within this research [37]. The stability and fluctuations of the conformational structure complex over a 100-ns duration are illustrated in Figure 8. The findings show that binding of the HL and $Co(HL)_2$ complexes to the 3KRR protein substantially enhances structural stability, as evidenced by essential dynamics analysis, which indicates a reduced conformational space compared to the unbound state. The RMSD analysis for the HL (Figure 8(a)) demonstrates that the HL molecule maintains its structural integrity without significant deviation. In Figure 8(c), it is observed that the $Co(HL)_2$ complex experiences slight diffusion from its initial binding site; however, the overall orientation and interaction patterns remain largely unaffected. The RMSF analysis reveals values below the threshold of 0.3 nm (Figure 8(b) and 8(d)), indicating the absence of significant conformational alterations along the protein chain as the HL integrates into the protein.

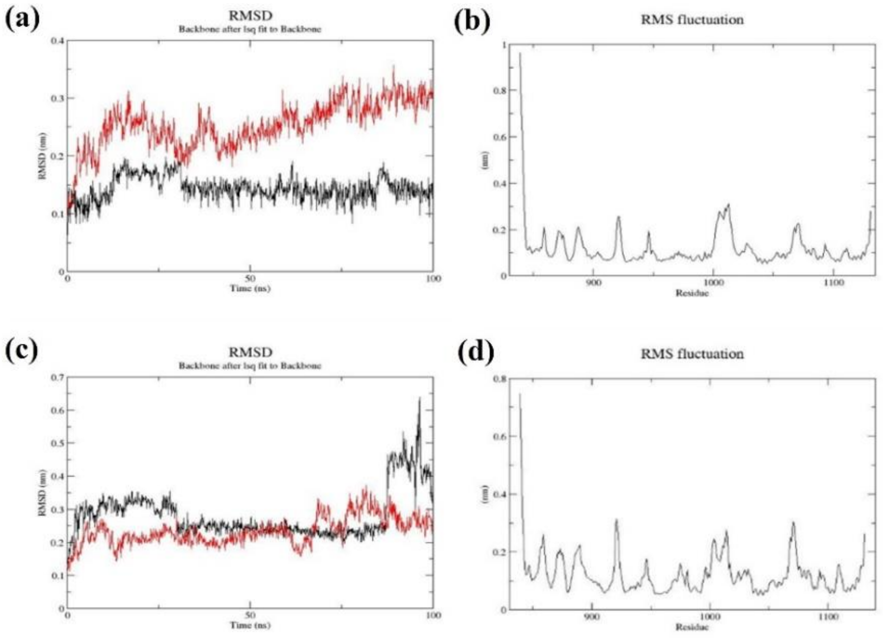

Figure 8. (a) RMSD graph of 3KRR-HL complex; **(b)** RMSF graph of 3KRR-HL complex; **(c)** RMSD graph of 3KRR-$Co(HL)_2$ complex; **(d)** RMSF graph of 3KRR-$Co(HL)_2$ complex.

The compactness of the protein was evaluated through an analysis of the radius of gyration (Figure 9(a) and Figure 9(c)) and solvent-accessible surface area (SASA) (Figure 9(b) and Figure 9(d)). The analysis of the radius of gyration indicates that overall fluctuations remained within 2.05-2.12 nm, a range that is relatively favorable for protein stability and structural integrity. Beyond the temporal threshold of 65 ns, fluctuations are further constrained to 2.125 nm; however, variations persist throughout the duration of the simulation. The initial SASA at 0 ns was recorded as 19742 nm^2, while at 100 ns it was observed to be approximately 165 nm^2. The SASA analysis revealed minimum, maximum, and mean values of roughly 145 nm^2, 170 nm^2, and 157 nm^2, respectively. A noticeable reduction in SASA values after 20 ns correlates with decreased fluctuations in the radius of gyration (Rg), indicating a more compact and stable protein–ligand complex over the simulation period.

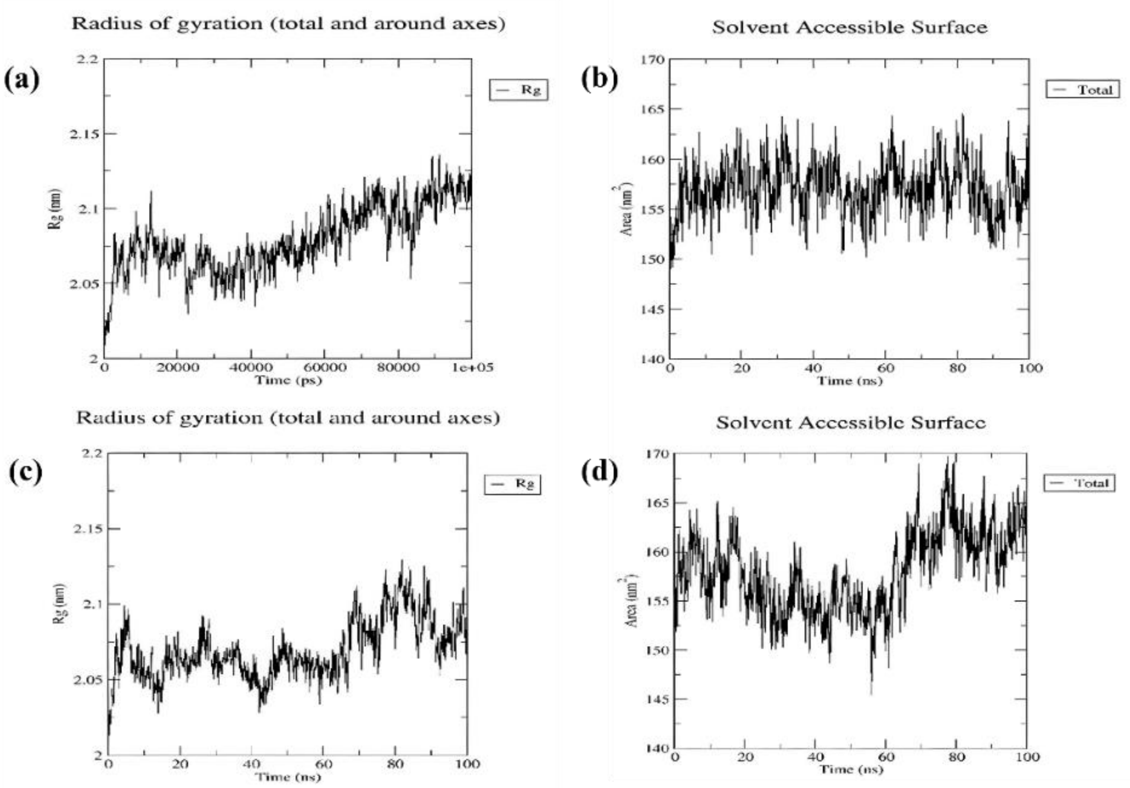

Figure 9. Molecular dynamics analysis of the 3KKR complexes: **(a)** Radius of gyration (Rg) profile of the 3KKR–HL complex; **(b)** Solvent-accessible surface area (SASA) of the 3KKR–HL complex; **(c)** Radius of gyration (Rg) profile of the 3KKR–Co(HL)$_2$ complex; **(d)** SASA profile of the 3KKR–Co(HL)$_2$ complex.

The Gibbs free energy landscape of the protein [Figure 10(a) and Figure 10(c)] throughout the simulation indicates substantial stability, as evidenced by the predominant coverage of the plot in dark blue, with only a minor portion in red. The dark blue coloration signifies a higher degree of stability, lower energy conditions, and a thermodynamically favorable state for the protein. In contrast, the red coloration signifies instability and elevated energy states of the protein. Intermolecular hydrogen bonding plays a key role in stabilizing the protein–ligand complex, as shown in Figure 10(b) and 10(d). During the simulation, the total number of hydrogen bonds, including both intra-protein and protein–ligand interactions, ranged from approximately 210 to 250, with an average of about 235. These consistent hydrogen-bonding interactions throughout the simulation indicate a stable, structurally maintained complex.

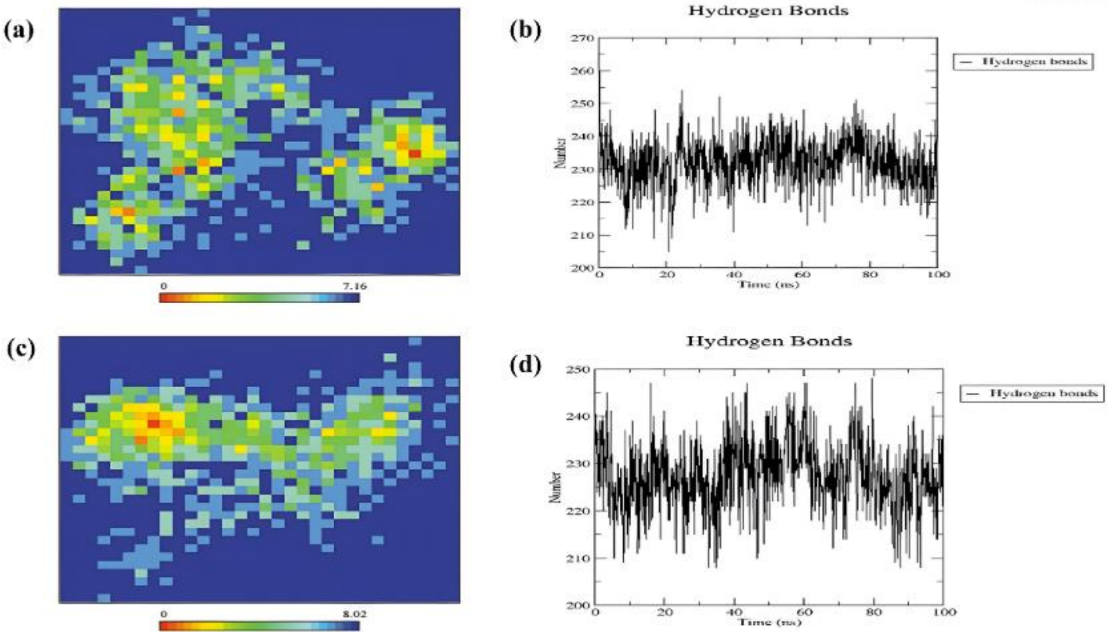

Figure 10. Molecular dynamics analysis of the 3KKR complexes: **(a)** Gibbs free energy landscape (FEL) of the 3KKR–HL complex; **(b)** Intermolecular hydrogen bond profile of the 3KKR–HL complex; **(c)** Gibbs free energy landscape (FEL) of the 3KKR–Co(HL)$_2$ complex; **(d)** Intermolecular hydrogen bond profile of the 3KKR–Co(HL)$_2$ complex.

4. Conclusions

In the current work, a novel ligand (HL) derived from dopamine, along with its corresponding metal complexes of Cu(II), Co(II), Ni(II), and Zn(II), was successfully synthesized and characterized utilizing spectroscopic, thermal, and structural analytical techniques. The ligand functioned as a bidentate donor, coordinating through its phenolic moiety. Among the synthesized metal complexes, Co(HL)$_2$ and Zn(HL)$_2$ demonstrated notable antiproliferative effects against the MDA-MB-231 and MDA-MB-468 breast cancer cell lines, with minimal cytotoxicity toward normal HEK-293 cells, highlighting their selective biological properties. Mechanistic investigations, including Hoechst/PI and Annexin V-FITC/PI staining, confirmed that apoptosis is the primary mechanism of cell death, and *in-silico* analyses revealed favorable interactions of these complexes within the ATP-binding domain of the JAK2 protein.

Author Contributions

Conceptualization, P.M.; methodology, M.H.C., P.M., and S.R.; software, N.G.N.; validation, P.M. and S.R.; formal analysis, M.H.C. and P.A.N.; investigation, M.H.C., P.A.N., S.M.S., S.R., and P.M.; resources, P.M. and S.R.; data curation, M.H.C., P.A.N., and N.G.N.; writing—original draft preparation, M.H.C. and P.A.N.; writing—review and editing, M.H.C., P.A.N., S.M.S., and P.M.; visualization, M.H.C., P.A.N., N.G.N., S.R., and P.M.; supervision, S.R. and P.M.; project administration, P.M.; funding acquisition, Y.Y. All authors have reviewed and approved the final version of the manuscript.

Institutional Review Board Statement

Not applicable.

Informed Consent Statement

Not applicable.

Data Availability Statement

All data generated or analysed during this study are included in this published article.

Funding

This work was supported by the VGST-CISEE Project (GRD No. 647), GOK, Karnataka, and also DST/KSTePS/Ph.D. Fellowship/CHE-05:2022-23/506.

Acknowledgments

The authors are grateful to SJCE, JSSSTU, Mysuru, for providing supercomputing facility and VGST-CISEE Project (GRD No. 647), Government of Karnataka, and DST/KSTePS/Ph.D. program Fellowship/CHE-05:2022-23/506 for financial assistance.

Conflicts of Interest

The authors declare that there are no conflicts of interest.

References

1. Cui, Y-Y. Cancer, Mankind′s Challenge. *Curr. Cancer Rep.* **2019**, *1*, 1–5, https://doi.org/10.25082/CCR.2019.01.001.
2. Takaidza, S.; Molefe, N.M.; Chihomvu, P. Molecular Basis of Cancer. In Clinical Applications of Cancer Genetic Testing, 1st Edition; Sharma, P., Ed.; CRC Press: Boca Raton, **2025**; https://doi.org/10.1201/9781003542162-2.
3. Uddin, N.; Rashid, F.; Ali, S.; Tirmizi, S.A.; Ahmad, I.; Zaib, S.; Zubair, M.; Diaconescu, P.L.; Tahir, M.N.; Iqbal, J. Synthesis, characterization, and anticancer activity of Schiff bases. *J. Biomol. Struct. Dyn.* **2020**, *38*, 3246-3259, https://doi.org/10.1080/07391102.2019.1654924.
4. Fox, S.; Speirs, V.; Shaaban, A.M. Male breast cancer: an update. *Virchows Arch.* **2022**, *480*, 85–93, https://doi.org/10.1007/s00428-021-03190-7.
5. Li, X.; Oprea-Ilies, G.M.; Krishnamurti, U. New developments in breast cancer and their impact on daily practice in pathology. *Arch. Pathol. Lab. Med.* **2017**, *141*, 490–8, https://doi.org/10.5858/arpa.2016-0288-SA.
6. Kennecke, H.; Yerushalmi, R.; Woods, R.; Cheang, M.C.U.; Voduc, D.; Speers, C.H.; Nielsen, T.O.; Gelmon, K. Metastatic behavior of breast cancer subtypes. *J. Clin. Oncol.* **2010**, *28*, 3271-3277, https://doi.org/10.1200/JCO.2009.25.9820.
7. Al-Mahmood, S.; Sapiezynski, J.; Garbuzenko, O.B.; Minko, T. Metastatic and triple-negative breast cancer: challenges and treatment options. *Drug Deliv. Transl. Res.* **2018**, *8*, 1483–507, https://doi.org/10.1007/s13346-018-0551-3.
8. Testa, U.; Castelli, G.; Pelosi, E. Breast Cancer: A Molecularly Heterogenous Disease Needing Subtype-Specific Treatments. *Med. Sci.* **2020**, 8, 18, https://doi.org/10.3390/medsci8010018.
9. Ginsburg, O.; Bray, F.; Coleman, M.P.; Vanderpuye, V.; Eniu, A.; Kotha, S.R.; Sarker, M.; Huong, T.T.; Allemani, C.; Dvaladze, A. The global burden of women’s cancers: a grand challenge in global health. *Lancet* **2017**, *389*, 847-860, https://doi.org/10.1016/S0140-6736(16)31392-7.
10. Winters, S.; Martin, C.; Murphy, D.; Shokar, N.K. Breast Cancer Epidemiology, Prevention, and Screening. *Prog. Mol. Biol. Transl. Sci.* **2017**, *151*, 1–32, https://doi.org/10.1016/bs.pmbts.2017.07.002.
11. Obeagu, E.I.; Obeagu, G.U. Breast cancer: A review of risk factors and diagnosis. *Medicine* **2024**, *103*, E36905, https://doi.org/10.1097/MD.0000000000036905.

12. Anastasiadi, Z.; Lianos, G.D.; Ignatiadou, E.; Harissis, H.V.; Mitsis, M. Breast cancer in young women: an overview. *Updates Surg*. **2017**, *69*, 313–317, https://doi.org/10.1007/s13304-017-0424-1.
13. Ferraro, M.G.; Piccolo, M.; Misso, G.; Santamaria, R.; Irace, C. Bioactivity and Development of Small Non-Platinum Metal-Based Chemotherapeutics. *Pharmaceutics* **2022**, *14*, 954, https://doi.org/10.3390/pharmaceutics14050954.
14. Ivanova, S. Metal-based organic complexes with anticancer activity. *Bulg. Soc. Med. Sci. J.* **2024**, *6*, e136135, https://doi.org/10.3897/bsms.6.136135.
15. Alka, Gautam. S.; Kumar, R.; Singh, P.; Gandhi. N.; Jain, P. Pharmacological aspects of Co(II), Ni(II) and Cu(II) schiff base complexes: An insight. *Results Chem.* **2023**, *5*, 100849, https://doi.org/10.1016/j.rechem.2023.100849.
16. Kovacic, P.; Osuna, J.A. Mechanisms of Anti-Cancer Agents: Emphasis on Oxidative Stress and Electron Transfer. *Curr. Pharm. Des*. **2000**, *6*, 277-309, https://doi.org/10.2174/1381612003401046.
17. Swathantraiah, J.G.; Srinivasa, S.M.; Belagal Motatis, A.K.; Uttarkar, A.; Bettaswamygowda, S.; Thimmaiah, S.B.; Niranjan, V.; Rangappa, S.; Subbegowda, R.K.; Ramegowda, T.N. Novel 1, 2, 5-trisubstituted benzimidazoles potentiate apoptosis by mitochondrial dysfunction in panel of cancer cells. *ACS Omega* **2022**, *7*, 46955-46971, https://doi.org/10.1021/acsomega.2c06057.
18. Shwetha, B.; Sudhanva, M.S.; Jagadeesha, G.; Thimmegowda, N.; Hamse, V.K.; Sridhar, B.; Thimmaiah, K.; Kumar, C.A.; Shobith, R.; Rangappa, K. Furan-2-carboxamide derivative, a novel microtubule stabilizing agent induces mitotic arrest and potentiates apoptosis in cancer cells. *Bioorg. Chem.* **2021**, *108*, 104586, https://doi.org/10.1016/j.bioorg.2020.104586.
19. Thomas, E.; Gopalakrishnan, V.; Hegde, M.; Kumar, S.; Karki, S.S.; Raghavan, S.C.; Choudhary, B. A novel resveratrol based tubulin inhibitor induces mitotic arrest and activates apoptosis in cancer cells. *Sci. Rep.* **2016**, *6*, 34653, https://doi.org/10.1038/srep34653.
20. Dhanalakshmi, B.; Anil Kumar, B.M.; Srinivasa Murthy, V.; Srinivasa, S.M.; Vivek, H.K.; Sennappan, M.; Rangappa, S. Design, synthesis and docking studies of novel 4-aminophenol-1, 2, 4-oxadiazole hybrids as apoptosis inducers against triple negative breast cancer cells targeting MAP kinase. *J. Biomol. Struct. Dyn.* **2024**, *42*, 5841-5857, https://doi.org/10.1080/07391102.2023.2239912.
21. Kabeer, F.A.; Rajalekshmi, D.S.; Nair, M.S.; Prathapan, R. Molecular mechanisms of anticancer activity of deoxyelephantopin in cancer cells. *Integr. Med. Res.* **2017**, *6*, 190–206, https://doi.org/10.1016/j.imr.2017.03.004.
22. Ejidike, I.P.; Direm, A.; Parlak, C.; Olaleru, S.A.; Adetunji, C.O.; Mtunzi, F.M.; Ata, A.; Eze, M.O.; Clayton, H.S.; Ajibade, P.A. DNA gyrase inhibition by Ni (II)-Schiff base complexes via in silico molecular docking studies: Spectroscopic, DFT calculations and in vitro pharmacological assessment. *Results Chem.* **2025**, *15*, 102219, https://doi.org/10.1016/j.rechem.2025.102219.
23. Pahonțu, E.; Proks, M.; Shova, S.; Lupașcu, G.; Ilieș, D.C.; Bărbuceanu, Ș.F.; Socea, L.I.; Badea, M.; Păunescu, V.; Istrati, D. Synthesis, characterization, molecular docking studies and in vitro screening of new metal complexes with Schiff base as antimicrobial and antiproliferative agents. *Appl. Organomet. Chem.* **2019**, *33*, e5185, https://doi.org/10.1002/aoc.5185.
24. Peng, Y.D.; Yan, Y.J.; La, Y.T.; Han, X.J.; Huang, F.; Dong, W.K. Two novel Cu(II) and Ni(II) quinolone-containing half-salamo-like complexes: Theoretical and experimental studies. *Inorg. Chem. Commun.* **2022**, *146*, 110121, https://doi.org/10.1016/j.inoche.2022.110121.
25. Karekal, M.R.; Mathada, M.B.H. Synthesis, spectroscopic characterization, and biological screening of binuclear transition metal complexes of bicompartmental Schiff bases containing indole and resorcinol moieties. *Turk. J. Chem.* **2013**, *37*, 775–95, https://doi.org/10.3906/kim-1303-28.
26. 1. Al-Shemary, R.K.; Mohapatra, R.K.; Kumar, M.; Sarangi, A.K.; Azam, M.; Tuli, H.S.; Ansari, A.; Mohapatra, P.K.; Dhama, K. Synthesis, structural investigations, XRD, DFT, anticancer and molecular docking study of a series of thiazole based Schiff base metal complexes. *J. Mol. Struct.* **2023**, *1275*, 134676, https://doi.org/10.1016/j.molstruc.2022.134676.
27. Nair, M.S.; Arish, D.; Joseyphus, R.S. Synthesis, characterization, antifungal, antibacterial and DNA cleavage studies of some heterocyclic Schiff base metal complexes. *J. Saudi Chem. Soc.* **2012**, *16*, 83–8, https://doi.org/10.1016/j.jscs.2010.11.002.
28. El-Shwiniy, W.H.; Ibrahim, A.G.; Sadeek, S.A.; Zordok, W.A. Synthesis, structural elucidation, molecular modeling and antimicrobial studies of 6-(2-hydroxyphenylimine)-2-thioxotetrahydropyrimidin-4(1H)-one (L) Schiff base metal complexes. *Appl. Organomet. Chem.* **2021**, *35*, e6174, https://doi.org/10.1002/aoc.6174.

29. Žukauskas, M.; Grybaitė, B.; Jonutė, P.; Vaickelionienė, R.; Gibieža, P.; Vaickelionis, G.; Dragūnaitė, B.; Anusevičius, K.; Mickevičius, V.; Petrikaitė, V. Evaluation of N-aryl-β-alanine derivatives as anticancer agents in triple-negative breast cancer and glioblastoma in vitro models. *Bioorg. Chem.* **2021**, *115*, 105214, https://doi.org/10.1016/j.bioorg.2021.105214.
30. Fisusi, F.A.; Akala, E.O. Drug combinations in breast cancer therapy. *Pharm. Nanotechnol.* **2019**, *7*, 3–23, https://doi.org/10.2174/2211738507666190122111224.
31. Li, Y.; Li, S.; Meng, X.; Gan, R.Y.; Zhang, J.J.; Li H, Bin. Dietary natural products for prevention and treatment of breast cancer. *Nutrients* **2017**, *9*, 728, https://doi.org/10.3390/nu9070728.
32. Wang, W.; Huang, S.; Li, S.; Li, X.; Ling, Y.; Wang, X.; Zhang, S.; Zhou, D.; Yin, W. Rosa sterilis Juice Alleviated Breast Cancer by Triggering the Mitochondrial Apoptosis Pathway and Suppressing the Jak2/Stat3 Pathway. *Nutrients* **2024**, *16*, 2784, https://doi.org/10.3390/nu16162784.
33. Lugano, R.; Ramachandran, M.; Dimberg, A. Tumor angiogenesis: causes, consequences, challenges and opportunities. *Cell. Mol. Life Sci.* **2020**, *77*, 1745–70, https://doi.org/10.1007/s00018-019-03351-7.
34. Carneiro, B.A.; El-Deiry, W.S. Targeting apoptosis in cancer therapy. *Nat. Rev. Clin. Oncol.* **2020**, *17*, 395–417, https://doi.org/10.1038/s41571-020-0341-y.
35. Jiang, D.; Xu, J.; Liu, S.; Nasser, M.I.; Wei, W.; Mao, T.; Liu, X.; Zou, X.; Li, J.; Li, X. Rosmanol induces breast cancer cells apoptosis by regulating PI3K/AKT and STAT3/JAK2 signaling pathways. *Oncol. Lett.* **2021**, *22*, 631, https://doi.org/10.3892/ol.2021.12892.
36. Yagil, Z.; Nechushtan, H.; Kay, G.; Yang, C.M.; Kemeny, D.M.; Razin, E. The enigma of the role of Protein inhibitor of Activated STAT3 (PIAS3) in the immune response. *Trends Immunol.* **2010**, *31*, 199–204, https://doi.org/10.1016/j.it.2010.01.005.
37. Ismail, N.Z.; Mohamed, W.A.S.; Ab. Rahim, N.; Hashim, N.M.; Adebayo, I.A.; Mohamad Zain, N.N.; Arsad, H. Molecular docking and molecular dynamic simulations of apoptosis proteins with potential anticancer compounds present in Clinacanthus nutans extract using gas chromatography–mass spectrometry. *J. Biomol. Struct. Dyn.* **2023**, *41*, 6104-6120, https://doi.org/10.1080/07391102.2022.2101530.

Publisher's Note & Disclaimer

Supplementary Materials

Table S1. Powder XRD data of Cu(HL)$_2$ complex.

Peak	2Θ	Θ	SinΘ	Sin^{2}Θ	Sin^{2}Θ /CF (h^2 + k^2 + l^2)	hkl	d		a in Å
							Obs	Cal	
1	18.60	9.30	0.1616	0.02611	1.0000 (1)	100	4.767	4.767	4.767
2	20.96	10.48	0.1819	0.03308	1.2669 (1)	100	4.235	4.235	4.235
3	37.81	18.90	0.3239	0.10492	4.0176 (4)	200	2.378	2.378	4.756
4	41.80	20.90	0.3567	0.12726	4.8730 (5)	210	2.159	2.159	4.828
5	45.57	22.78	0.3872	0.14992	5.7407 (6)	211	1.989	1.989	4.873
6	68.14	34.07	0.5602	0.31382	12.0172 (12)	222	1.375	1.375	4.763

Table S2. Powder XRD data of Co(HL)$_2$ complex.

Peak	2Θ	Θ	SinΘ	Sin^{2}Θ	Sin^{2}Θ /CF (h^2 + k^2 + l^2)	hkl	d		a in Å
							Obs	Cal	
1	12.70	6.35	0.1106	0.01223	1.0000 (1)	100	6.965	6.965	6.965
2	21.20	10.60	0.1840	0.03384	2.7662 (3)	111	4.188	4.188	7.253
3	29.50	14.75	0.2546	0.06482	5.2991 (5)	210	3.026	3.026	6.765
4	33.20	16.60	0.2857	0.08162	6.6721 (7)	-	2.696	2.696	7.134
5	36.30	18.15	0.3115	0.09704	7.9325 (8)	220	2.473	2.473	6.994
6	43.30	21.65	0.3689	0.13611	11.1270 (11)	311	2.088	2.088	6.925
7	48.60	24.30	0.4115	0.16934	13.8435 (13)	321	1.872	1.872	7.004
8	58.70	29.35	0.4901	0.24024	19.6392 (20)	420	1.572	1.572	7.028
9	66.70	33.35	0.5498	0.30223	24.7064 (25)	421	1.401	1.401	7.006

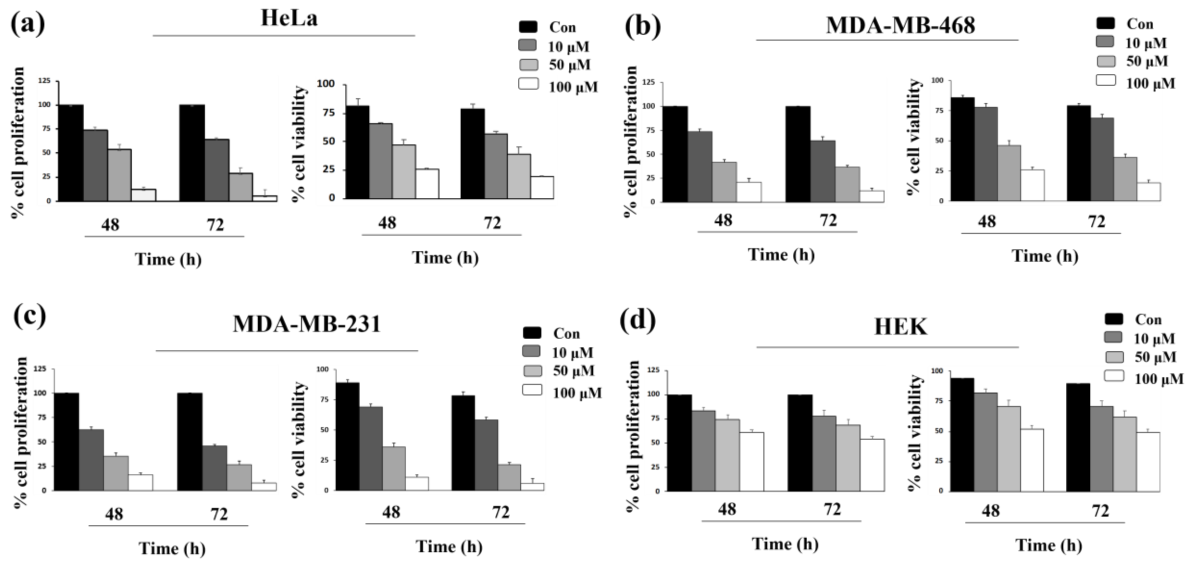

Figure S1. Effect of Zn(HL)$_2$ complex on cell proliferation and viability; **(a)** HeLa cells treated with Co(HL)$_2$ (10, 50 and 100 µM) for 48 and 72 h, assessed by MTT and Trypan Blue assays; **(b)** MDA-MB-468 cells treated under identical conditions showing dose- and time-dependent reduction in viability; **(c)** MDA-MB-231 cells exhibiting decreased proliferation and viability with increasing Zn(HL)$_2$ concentrations; **(d)** Normal HEK-293 cells showing minimal cytotoxicity even at higher Zn(HL)$_2$ doses, confirming selective toxicity toward cancer cells. Data represent mean ± SD from three independent experiments; DMSO-treated cells served as vehicle controls.

Table S3. Powder XRD data of Ni(HL)$_2$ complex.

Peak	2Θ	Θ	SinΘ	Sin^{2}Θ	Sin^{2}Θ /CF (h^2 + k^2 + l^2)	hkl	d		a in Å
							Obs	Cal	
1	22.60	11.30	0.1959	0.03839	1.0000 (1)	100	3.931	3.931	3.931
2	34.90	17.45	0.2999	0.08992	2.3421 (2)	110	2.569	2.569	3.633
3	43.90	21.95	0.3738	0.13972	3.6391 (4)	200	2.061	2.061	4.121
4	54.10	27.05	0.4548	0.20681	5.3865 (5)	210	1.694	1.694	3.788
5	60.90	30.45	0.5068	0.25683	6.6892 (7)	-	1.520	1.520	4.021
6	67.60	33.80	0.5563	0.30946	8.0601 (8)	220	1.385	1.385	3.917
7	72.70	36.35	0.5927	0.35131	9.1500 (9)	221	1.300	1.300	3.899

Table S4. Powder XRD data of $Zn(HL)_2$ complex.

Peak	2Θ	Θ	SinΘ	$Sin^2Θ$	$Sin^2Θ$ /CF ($h^2 + k^2 + l^2$)	hkl	d		a in Å
							Obs	Cal	
1	23.10	11.55	0.2002	0.04009	1.0000 (1)	100	3.847	3.847	3.847
2	33.10	16.55	0.2849	0.08114	2.0240 (2)	110	2.704	2.704	3.824
3	38.20	19.10	0.3272	0.10707	2.6708 (3)	111	2.354	2.354	4.077
4	47.60	23.80	0.4035	0.16285	4.0622 (4)	200	1.909	1.909	3.818
5	59.10	29.55	0.4932	0.24323	6.0672 (6)	211	1.562	1.562	3.826
6	69.20	34.60	0.5678	0.32245	8.0432 (8)	220	1.357	1.357	3.837
7	77.70	38.85	0.6273	0.39348	9.8152 (10)	310	1.228	1.228	3.883

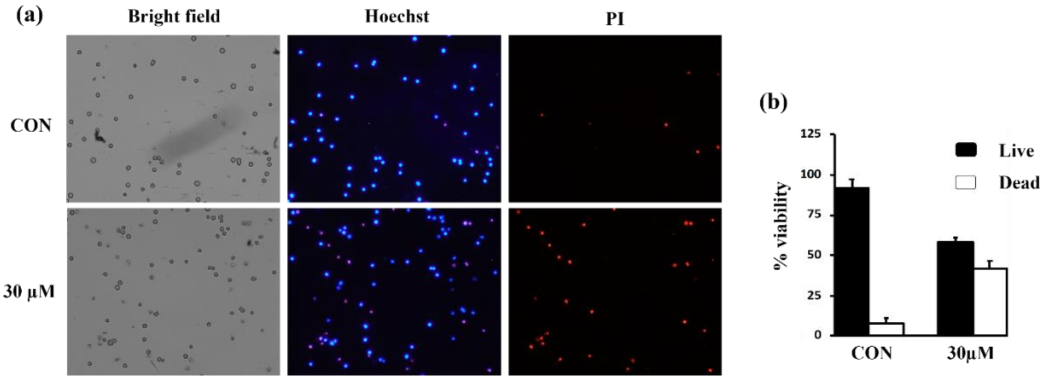

Figure S2. Induction of apoptosis in MDA-MB-231 cells by $Zn(HL)_2$ complex: **(a)** Bright-field, Hoechst, and PI images of control and 30 µM $Zn(HL)_2$-treated cells after 24 h; **(b)** Percentage of live and dead cells quantified from Hoechst/PI staining (mean ± SD, n = 3; ≥500 cells counted).

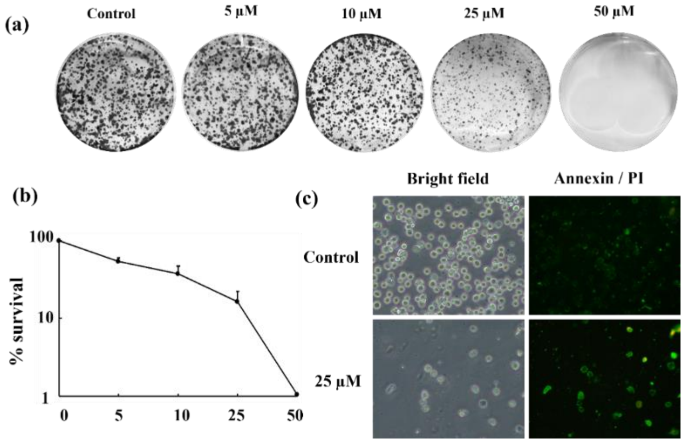

Figure S3. Effect of $Zn(HL)_2$ complex on colony formation capability: MDA-MB-231 cells were treated with different concentrations of $Zn(HL)_2$ complex and subjected to survival and apoptotic analysis **(a)** crystal violet stained colonies; **(b)** percentage survival graph; **(c)** Annexin PI stained cells.